Magnetoresistance and Magnetic Ordering Fingerprints in Hydrogenated Graphene

David Soriano,[1,2] Nicolas Leconte,[3] Pablo Ordejón,[4] Jean-Christophe Charlier,[3] Juan-Jose Palacios,[5] and Stephan Roche[6,7]

[1]*Departamento de Física Aplicada, Universidad de Alicante, San Vicente del Raspeig, Alicante 03690, Spain*
[2]*Instituto de Ciencia de Materiales de Madrid (CSIC), Cantoblanco, Madrid, 28049, Spain*
[3]*Université Catholique de Louvain, Institute of Condensed Matter and Nanoscience (IMCN), Place Croix du Sud 1 (NAPS-Boltzmann), 1348 Louvain-la-Neuve, Belgium*
[4]*CIN2 (CSIC-ICN) Barcelona, Campus Universitat Autonoma de Barcelona, E-08193 Bellaterra, Spain*
[5]*Departamento de Física de la Materia Condensada, Universidad Autónoma de Madrid, Cantoblanco, Madrid, 28049, Spain*
[6]*CIN2 (ICN-CSIC) and Universitat Autonoma de Barcelona, Catalan Institute of Nanotechnology, Campus de la UAB, 08193 Bellaterra (Barcelona), Spain*
[7]*ICREA, Institució Catalana de Recerca i Estudis Avançats, 08010 Barcelona, Spain*

(Received 20 January 2011; published 30 June 2011)

Spin-dependent features in the conductivity of graphene, chemically modified by a random distribution of hydrogen adatoms, are explored theoretically. The spin effects are taken into account using a mean-field self-consistent Hubbard model derived from first-principles calculations. A Kubo transport methodology is used to compute the spin-dependent transport fingerprints of weakly hydrogenated graphene-based systems with realistic sizes. Conductivity responses are obtained for paramagnetic, antiferromagnetic, or ferromagnetic macroscopic states, constructed from the mean-field solutions obtained for small graphene supercells. Magnetoresistance signals up to ~7% are calculated for hydrogen densities around 0.25%. These theoretical results could serve as guidance for experimental observation of induced magnetism in graphene.

DOI: 10.1103/PhysRevLett.107.016602 PACS numbers: 72.80.Vp, 73.20.Hb, 85.75.−d

Introduction.—Close to the charge neutrality point, two-dimensional graphene exhibits fascinating transport properties deriving from the massless Dirac fermions physics [1,2]. These electronic properties can be further tuned and diversified through chemical functionalization [3] or irradiation (defects formation) [4]. Indeed, strong modifications of the sp^2-bonded carbon network by grafting sp^3-type defects is, for instance, an interesting strategy to induce an insulating behavior in graphene. Following this idea, recent attempts based on hydrogenation and fluorination were able to turn graphene into a wide band-gap insulator [5,6].

While ideal bidimensional graphene is nonmagnetic, its unidimensional derivatives (graphene nanoribbons) could exhibit magnetic ordered states due to the presence of edges [7]. Additionally, monovacancies or sp^3-type defects (such as those created by adsorbed atomic H) can introduce local sublattice imbalances in graphene, thus inducing magnetic moments [8,9] according to Lieb's theorem [10]. Experimentally, the existence of intrinsic magnetism in graphene and graphite-based materials is strongly debated [11,12]. Some experimental works assume that the observed magnetic ordering is coming from graphene edges or grain boundaries [12], a scenario that has been recently questioned by Sepioni and coworkers who found no magnetism even for a high concentration of edge defects [13]. In several recent experiments [14], signatures of room temperature ferromagnetism in graphene were tentatively related to the presence of hydrogen impurities. We note that in all those experiments, the nature and quantity of defects remain poorly characterized and mostly uncontrolled. It would be consequently highly desirable to clarify the conditions for observing spin-dependent transport fingerprints in hydrogenated graphene.

In this Letter, spin-dependent transport properties of hydrogenated graphene-based systems with realistic sizes are explored theoretically. Firstly, a spin-dependent one-orbital Hubbard Hamiltonian, describing adsorbed hydrogen impurities on a graphene sheet, is derived using first-principles calculations and solved at a mean-field level. The local spin texture around hydrogen adatoms is found to be strongly dependent on both the concentration and the specific adsorption sublattice of neighboring adatoms as previously reported [9,15]. The self-consistent Hubbard Hamiltonian is then implemented into a real space (Kubo)-transport method. Our theoretical results reveal the suitable hydrogenation coverage of graphene to maximize spin-dependent conductivities, which translate into measurable magnetoresistance signals in the diffusive regime.

Single-orbital mean-field Hubbard approximation.—The single-orbital tight-binding description of graphene restricts to p_z orbitals centered on each carbon atom. The spin-related physics induced by Coulomb interaction is introduced by means of the Hubbard model in its mean-field approximation

$$\mathcal{H} = t\sum_{\langle i,j\rangle,\sigma} c^{\dagger}_{i,\sigma}c_{j,\sigma} + U\sum_{i} n_{i,\uparrow}\langle n_{i,\downarrow}\rangle + n_{i,\downarrow}\langle n_{i,\uparrow}\rangle, \qquad (1)$$

where t is the first-neighbor hopping term, $c^{\dagger}_{i,\sigma}$ ($c_{j,\sigma}$) is the creation (annihilation) operator in the lattice site i (j) with spin σ, U is the on-site Coulomb repulsion, and $n_{i,\downarrow}$, $n_{i,\uparrow}$ are the self-consistent occupation numbers for spin-down and spin-up electrons, respectively. When a hydrogen (H) atom is adsorbed on top of a carbon (C) atom, the sp^2 symmetry is locally broken, and the electron from the C p_z orbital is removed from the π bands to form a σ bond with the H atom. Consequently, within the *tight-binding* approximation, such an adsorption is modeled by removing the corresponding electron and lattice site [as illustrated in Fig. 1(a)]. Figure 1(b) presents one of the supercells ($N = 791$ atomic sites) used in periodic boundary conditions calculations. This hydrogen defect induces zero-energy electronic states which are mainly localized around the impurity [11,16]. When the Coulomb repulsion is switched on in the calculation, these zero-energy states spin-polarize, leading to semilocal $S = 1/2$ magnetic moments with a staggered spin density mostly located on one sublattice [8,9,15] [see Figs. 2(a) and 2(d)]. When a finite concentration of defects is present, the magnetic ordering between these magnetic moments is dictated by the sublattices where they are located, being copolarized or ferromagnetic (FM) for the same sublattice and counterpolarized or antiferromagnetic (AF) otherwise [Fig. 2(b) and 2(e)].

Magnetic states.—The total spin S of the macroscopic ground state is given by the excess of magnetic moments on one specific sublattice, although $S = 0$ is the most likely value on simple statistical grounds (equal H occupation of both sublattices). In the following, two assumptions related to the macroscopic magnetic states are considered. The first one is the simplest: a *paramagnetic* (PM) state, which is a good approximation for sufficiently low H concentrations, or at sufficiently high temperatures, in which there is no correlation between the semilocal moments. This state is thus constructed from independent large supercells containing a single vacancy as shown in Fig. 1(b). The corresponding spin densities on each cell site are represented in Figs. 2(a) and 2(d) as a function of the distance to the center of the supercell for two different concentrations of defects. The result favorably compares with first-principles calculations when $U/t = 1$ [17].

The second assumption is more complex since pairwise magnetic ordered states are investigated. The latter are constructed using supercells containing two vacancies on different sublattices [see Fig. 1(c)] far from the edges [18]. When selecting one site on each sublattice [see Fig. 1(b) and 1(e)], the magnetic moments couple antiferromagnetically and the macroscopic state generated by merging several supercells is an antiferromagnet with zero total spin ($S = 0$). We explore the effect of the distance (d) between vacancies while varying accordingly the supercell size. By changing simultaneously the distance and size, we always allow for a meaningful definition for the concentration n_x based on only two vacancies per cell. One notes that for $n_x = 0.6\%$ ($d = 8.5$ Å) the vacancies become very close to each other, thus allowing overlapping between magnetic moments and suppression of the local antiferromagnetic state [9]. We note that, when the vacancies are in the same sublattice, the ground state is ferromagnetic (FM), but we will not consider this case in this work (see [19]).

The AF ordering can be further tuned by applying a sufficiently large external magnetic field, parallel to the

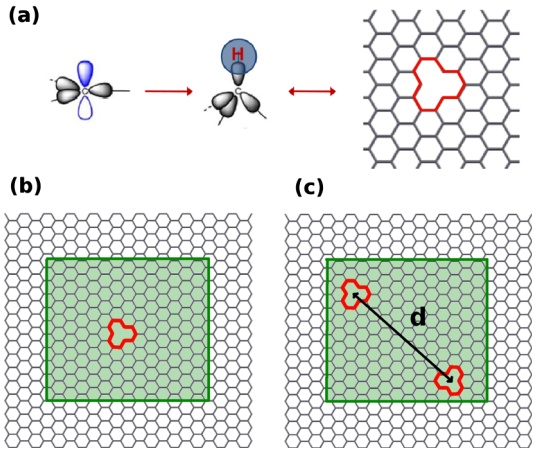

FIG. 1 (color online). (a) Schematic representation of the sp^2 hybridization breakdown upon hydrogen adsorption. In our tight-binding model, such a defect is mimicked by a monovacancy. (b) Single-vacancy supercell used in the mean-field Hubbard model calculations with periodic boundary conditions. (c) Supercell with two vacancies. The distance between two hydrogen defects is labeled by (d). The green shaded regions give the space location for the defects, to minimize the correlations between vacancies in neighboring cells.

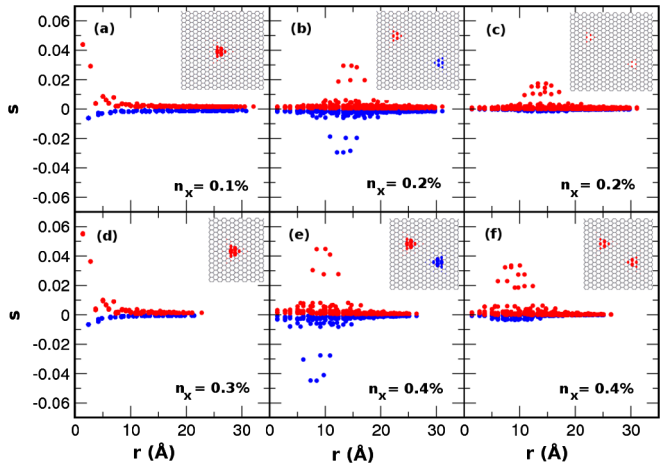

FIG. 2 (color online). Local (site) spin (s) versus r (the distance to the center of the supercell) for various vacancy concentrations: (a),(d) $n_x = 0.1\%$ and 0.3% in the paramagnetic case, (b),(e) $n_x = 0.2\%$ ($d = 27.7$ Å) and 0.4% ($d = 18.1$ Å) in an antiferromagnetic state, and (c),(f) in a ferromagnetic excited state within the mean-field Hubbard approximation [↑ (red [medium gray]) and ↓ (blue [dark gray]) electrons]. In all cases, the center of mass of the vacancies is at $r = 0$.

graphene sample. First-principles calculations performed with the SIESTA code [20], for the unit cell shown in Fig. 2(b), reveal that the energy difference between the antiferromagnetic and ferromagnetic configurations is about 1 meV, yielding a rough value of ten Tesla for the corresponding switching magnetic field (smaller values are expected for smaller H concentrations). Similar values were predicted for hydrogenated graphene nanoribbons although with larger interdistance between H adatoms [15] and also for monovacancies in carbon nanotubes [21]. When applying the magnetic field, the local magnetic moments become copolarized giving rise to a FM state. The difference in the magnetic ordering can affect the conductivity and induce a magnetoresistive (MR) response as discussed for graphene nanoribbons in Ref. [15]. To study the possible magnetoresistance signals in hydrogenated graphene samples, the spin density and related spin-dependent on-site energies have been computed for this specific case [Figs. 2(c) and 2(f)].

Kubo conductivity methodology.—Using the self-consistent Hubbard Hamiltonian calculations, spin-dependent on-site energies are estimated for each supercell. These *tight-binding* parameters are then used for computing the conductivity in realistic-sized samples applying the Kubo formalism. These graphene samples are constructed by attaching a large number of these supercells following different random arrangements. An efficient real space order N method is then used to simultaneously follow the wave packet dynamics and to compute the Kubo conductivity (see Refs. [22] for details). The analysis of the wave packet dynamics allows us to extract the conduction mechanisms and transport length scales (mean free path). As long as $n_x \leq 0.5\%$ the diffusion coefficients are found to reach a saturation regime after a few thousands of femtoseconds, and then remain roughly constant up to very long times, indicating a diffusive regime and a negligible contribution of quantum interferences within the computational reach. The maximum value allows the evaluation of $\ell_e = D_{\max}/v_F$, with $v_F = 10^6$ ms^{-1}. Note that the transport properties are calculated in the zero temperature limit, which should, however, be robust to higher temperatures given the weak electron-phonon coupling in graphene.

Spin-dependent transport features.—The scaling analysis of the conductivity is carried out using the Kubo formula $\sigma_{\uparrow,\downarrow}(E,t) = (e^2/2)\mathrm{Tr}[\delta_{\uparrow,\downarrow}(E-\hat{H})]D_{\uparrow,\downarrow}(E,t)$ where $\mathrm{Tr}[\delta_{\uparrow,\downarrow}(E-\hat{H})/S]$ are the spin-dependent density of states per unit of surface at the energy E. At a fixed energy, $\sigma_{\uparrow,\downarrow}(E,t)$ reach their maximal values at the same time as $D_{\uparrow,\downarrow}(E,t)$ $(D^{\max}_{\uparrow,\downarrow})$ which gives the spin-dependent Drude conductivities $\sigma^{\mathrm{Drude}}_{\uparrow,\downarrow}(E) = (e^2/2)\mathrm{Tr}[\delta_{\uparrow,\downarrow}(E-\hat{H})]D^{\max}_{\uparrow,\downarrow}(E)$, that account for the disorder effects on the density of states.

Figure 3 presents the Drude conductivities for the AF case (left panel), FM case (right panel) and the approximated PM case (inset in right panel) for H concentrations

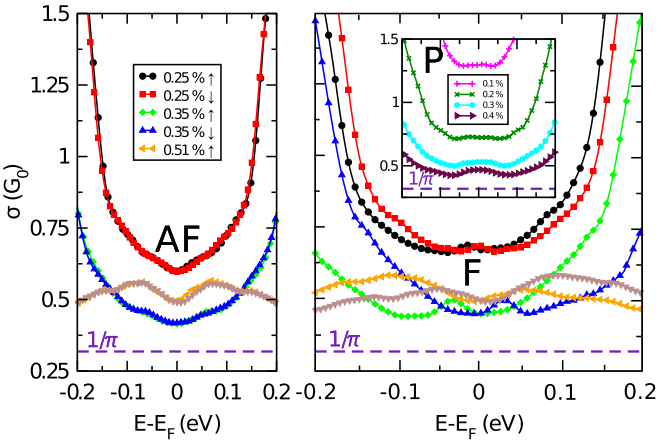

FIG. 3 (color online). Left panel : Conductivities of hydrogenated graphene samples with various concentrations for the antiferromagnetic case (left panel), paramagnetic case (right panel inset) and ferromagnetic case (right panel main frame). Dashed lines give $2e^2/\pi h$.

varying from 0.1% up to 0.5%. As expected, both in the AF and the PM case, no spin-dependent transport features are observed in the results, with the conductivities for up and down spins being equal within the statistical error. We note, however, some differences in the shape of the conductivity curves versus energy close to the Dirac point between the PM and AF cases. In sharp contrast, in the FM case, the spin-dependent conductivities significantly differ away from the charge neutrality point, with $|\sigma^{\mathrm{Drude}}_{\uparrow}(E)/\sigma^{\mathrm{Drude}}_{\downarrow}(E)|$ typically increasing with energy. $\sigma^{\mathrm{Drude}}_{\uparrow,\downarrow}(E)$ decays roughly linearly with n_x for the lowest H density (which is a trend in general for resonant scattering [23]), but one clearly observes a tendency towards saturation at higher concentration. It is worth mentioning that, in all cases, the total Drude conductivities $(\sigma^{\mathrm{Drude}}_{\uparrow}(E) + \sigma^{\mathrm{Drude}}_{\downarrow}(E))$ remain larger than $2G_0/\pi = 4e^2/\pi h$, which is the theoretical minimum value estimated within the self-consistent Born approximation [24].

From the computed conductivities in the AF and FM cases, one extracts (for AB-sublattice preserved symmetry), the magnetoresistance $\mathrm{MR} = (\sigma^F - \sigma^{\mathrm{AF}})/(\sigma^F + \sigma^{\mathrm{AF}})$, with $\sigma^F = \sigma^F_{\uparrow} + \sigma^F_{\downarrow}$ and $\sigma^{\mathrm{AF}} = \sigma^{\mathrm{AF}}_{\uparrow} + \sigma^{\mathrm{AF}}_{\downarrow}$. Figure 4 shows the magnetoresistance for three different H concentrations. The maximum signal is observed for the lowest density $n_x = 0.25\%$ and reaches about 7% for a switch from the antiferromagnetic to the excited ferromagnetic case. The signal is reduced with increasing n_x and tends to disappear at higher concentrations, along with the spin density. One also notes that, since the macroscopic states are built out of supercells carrying only two vacancies, the number of magnetic correlations is likely underestimated. Hence, experimental observations of larger MR values would not be a surprise. We observe some asymmetry in the MR profiles (Fig. 4) which stems from small numerical inaccuracies due to both, the approximated Hubbard Hamiltonian and the use of a random phase

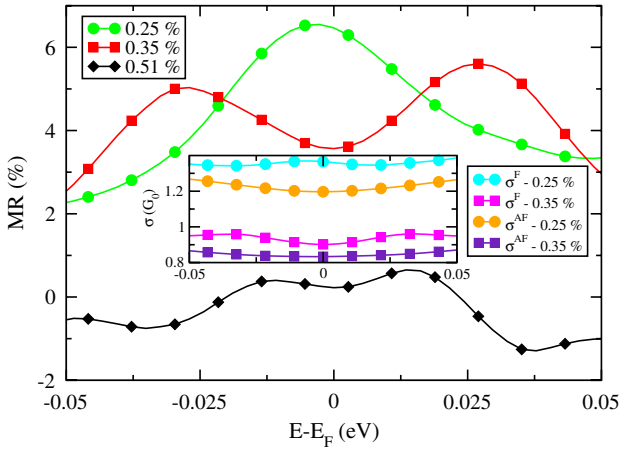

FIG. 4 (color online). Magnetoresistance of hydrogenated graphene samples with concentrations of $n_x = 0.25, 0.35, 0.5\%$ as a function of Fermi level position. Inset : Conductivities for the ferromagnetic and antiferromagnetic graphene samples at densities of $n_x = 0.25, 0.35\%$.

approximation for the Kubo methodology. Figure 4 (inset) also emphasizes the energy-dependent conductivities for $n_x = 0.25\%$ and $n_x = 0.35\%$ close to the Fermi level, which result in the qualitatively different profiles observed in the energy-dependent MR signals.

Conclusion.—We have reported the first numerical evidence of how the existence and relative orientation of the magnetic moments can be manifest in a standard magnetoconductivity measurement of large hydrogenated graphene flakes. Given the current difficulty to probe intrinsic magnetism in graphene with other experimental techniques, our results definitely point towards magnetoresistance as the smoking gun of such an elusive and controversial phenomenon.

Spanish Grants from MICINN to D. S. and J. J. P. (FIS2010-21883-C02-02, CSD2007-00010) and P. O. (FIS2009-12721-C04-01, CSD2007-00050) are acknowledged. D. S. acknowledges the Universidad de Alicante, a CSIC PhD Grant, and J. Fernández-Rossier. This work is connected to the Belgian Program on Interuniversity Attraction Poles (PAI6), the ARC on "Graphene, " the ETSF e-I3 project (Grant No. 211956) and the Belgium FNRS.

[1] A. K. Geim and K. S. Novoselov, Nature Mater. **6**, 183 (2007).
[2] A. H. Castro Neto *et al.*, Rev. Mod. Phys. **81**, 109 (2009); D. S. L. Abergel *et al.*, Adv. Phys. **59**, 261 (2010).
[3] K. P. Loh *et al.*, J. Mater. Chem. **20**, 2277 (2010).
[4] A. V. Krasheninnikov and F. Banhart, Nature Mater. **6**, 723 (2007).
[5] D. C. Elias *et al.*, Science **323**, 610 (2009); A. Bostwick *et al.*, Phys. Rev. Lett. **103**, 056404 (2009); J. Katoch *et al.*, Phys. Rev. B **82**, 081417(R) (2010).
[6] S. H. Cheng *et al.*, Phys. Rev. B **81**, 205435 (2010); F. Withers, M. Dubois, and A. K. Savchenko, Phys. Rev. B **82**, 073403 (2010).
[7] Y.-W. Son, M. L. Cohen, and S. G. Louie, Phys. Rev. Lett. **97**, 216803 (2006); J. Fernández-Rossier and J. J. Palacios, Phys. Rev. Lett. **99**, 177204 (2007).
[8] O. V. Yazyev and L. Helm, Phys. Rev. B **75**, 125408 (2007); O. V. Yazyev, Phys. Rev. Lett. **101**, 037203 (2008); Rep. Prog. Phys. **73**, 056501 (2010).
[9] Y.-W. Son, M. L. Cohen, and S. G. Louie, Nature (London) **444**, 347 (2006).
[10] E. H. Lieb, Phys. Rev. Lett. **62**, 1201 (1989).
[11] M. M. Ugeda *et al.*, Phys. Rev. Lett. **104**, 096804 (2010).
[12] P. Esquinazi *et al.*, Phys. Rev. Lett. **91**, 227201 (2003); J. Cervenka, M. I. Katsnelson, and C. F. J. Flipse, Nature Phys. **5**, 840 (2009); D. Martinez-Martin *et al.*, Phys. Rev. Lett. **105**, 257203 (2010).
[13] M. Sepioni *et al.*, Phys. Rev. Lett. **105**, 207205 (2010).
[14] H. Ohldag *et al.*, New J. Phys. **12**, 123012 (2010); A. Candini *et al.*, Phys. Rev. B **83**, 121401(R) (2011); L. Xie *et al.*, Appl. Phys. Lett. **98**, 193113 (2011).
[15] D. Soriano *et al.*, Phys. Rev. B **81**, 165409 (2010).
[16] N. M. R. Peres, F. Guinea, and A. H. Castro Neto, Phys. Rev. B **73**, 125411 (2006).
[17] The CRYSTAL *ab initio* package has been employed using the Perdew-Burke-Ernzerhof (PBE) exchange-correlation functional. The geometry of a single H atom adsorbed on the supercell has been relaxed locally to obtain the typical sp^3 configuration. For C atoms, a valence basis set ($2s$, $2p$) is used with the core electrons replaced by a pseudopotential. The STO-3G basis set was chosen to describe the $1s$ orbital of the H atoms. The standard deviation of the total magnetic moment inside each supercell $\Sigma = \sqrt{\sum_{i=1}^{n} s_i^2}$ gives similar results with both methods: $\Sigma_{\text{Hubbard}} = 0.124$, taking $U/t = 1$ (see L. Pisani, J. A. Chan, B. Montanari, and N. M. Harrison, Phys. Rev. B **75**, 064418 (2007)), and $\Sigma_{\text{DFT}} = 0.154$.
[18] Because of the zero-energy wave-function decay close to a hydrogen adatom in graphene, $\Psi \propto 1/\mathbf{r}$, the supercell size is chosen large enough to avoid interaction between magnetic moment localized around the defect and its periodic images in neighboring cells. Convergence is achieved when on-site energies tend to $U/2$ and when the spin density approaches zero near the supercell border. Although the spin density never truly vanishes near the border, its value can be neglected for the considered vacancy concentrations.
[19] N. Leconte *et al.*, ACS Nano **5**, 3987 (2011).
[20] E. Artacho *et al.*, Phys. Status Solidi B **215**, 809 (1999).
[21] Z. Zanolli and J. C. Charlier, Phys. Rev. B **81**, 165406 (2010).
[22] S. Roche and D. Mayou, Phys. Rev. Lett. **79**, 2518 (1997); H. Ishii *et al.*, C.R. Physique **10**, 283 (2009); N. Leconte *et al.*, ACS Nano **4**, 4033 (2010).
[23] T. O. Wehling *et al.*, Phys. Rev. Lett. **105**, 056802 (2010); P. M. Ostrovsky *et al.*, Phys. Rev. Lett. **105**, 266803 (2010); M. Titov *et al.*, Phys. Rev. Lett. **104**, 076802 (2010).
[24] P. M. Ostrovsky, I. V. Gornyi, and A. D. Mirlin, Phys. Rev. B **74**, 235443 (2006); K. Nomura and A. H. MacDonald, Phys. Rev. Lett. **98**, 076602 (2007).